J. Fluid Mech. (1997), *vol.* 332, *pp.* 41–70

The horseshoe vortex and vortex shedding around a vertical wall-mounted cylinder exposed to waves

By B. M. SUMER, N. CHRISTIANSEN AND J. FREDSØE

Technical University of Denmark, Department of Hydrodynamics and Water Resources, 2800 Lyngby, Denmark

(Received 8 February 1996 and in revised form 3 July 1996)

This study concerns the flow around the base of a vertical, wall-mounted cylinder – a pile – exposed to waves. The study comprises (i) flow visualization of horseshoe-vortex flow in front of and the lee-wake-vortex flow behind the pile and (ii) bed shear stress measurements around the pile conducted in a wave flume, plus supplementary bed shear stress measurements carried out in an oscillatory-flow water tunnel. The Reynolds number range of the flume experiments is $Re_D = (2\text{–}9) \times 10^3$ and that of the tunnel experiments is $Re_D = 10^3\text{–}5 \times 10^4$, in which Re_D is based on the pile size. Steady-current tests were also carried out for reference. The horseshoe-vortex flow (like lee-wake-vortex flow) is governed primarily by the Keulegan–Carpenter number, KC. The range of KC was from 0 to about 25 in the flume experiments, and from 4 to 120 in the tunnel experiments. The experiments were conducted mainly with circular piles. The results indicate that no horseshoe vortex exists for $KC < 6$. The size and lifespan of the horseshoe vortex increase with KC. The influence of the cross-sectional shape of the pile on the horseshoe vortex was investigated. The results show that a square pile with 90° orientation produces the largest horseshoe vortex while that with 45° orientation produces the smallest one, the circular-pile result being between the two. The influence of a superimposed current on the horseshoe vortex was also investigated. The range of the current-to-wave-induced-velocity ratio, U_c/U_m, was from 0 to about 0.8. The overall effect of the superimposed current is to increase the size and lifespan of the horseshoe vortex. This effect increases with increasing U_c/U_m. Regarding the near-bed lee-wake flow, the flow regimes observed for the two-dimensional free-cylinder case exist for the present case, too, but with one exception: in the present case, no transverse vortex street was observed in the so-called single-pair regime. The results show that the bed shear stress beneath the horseshoe vortex and in the lee-wake area is heavily influenced by KC. The amplification of the bed shear stress with respect to its undisturbed value is maximum ($O(4)$) at the side edges of the pile, in contrast to what occurs in steady currents where the maximum occurs at an angle of about 45° from the upstream edge of the pile with an amplification of $O(10)$.

1. Introduction

The flow around the base of a vertical pile consists of two basic flow structures: one is the so-called horseshoe vortex which is formed in front of the pile, and the other is the vortex flow pattern formed at the lee side of it (figure 1).

The horseshoe vortex is caused by the rotation in the incoming flow: the boundary layer on the bed, upstream of the pile, undergoes a three-dimensional separation under the influence of the adverse pressure gradient produced by the pile, and the separated

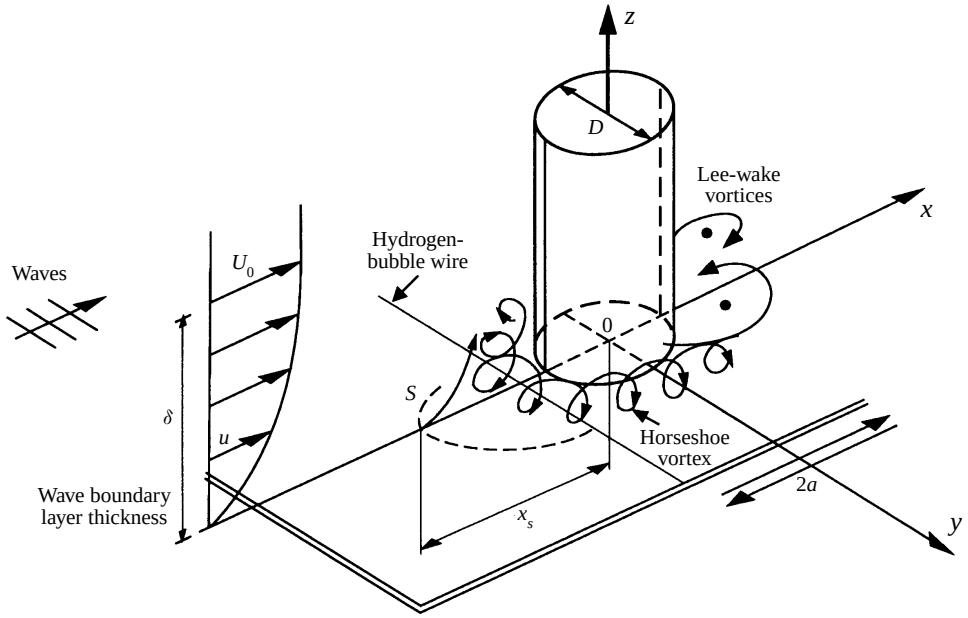

FIGURE 1. Definition sketch. S: separation line.

boundary layer rolls up to form a swirling vortex around the pile, which then trails off downstream (figure 1).

The lee-side vortices, on the other hand, are caused by the rotation in the boundary layer over the surface of the pile: the shear layers emanating from the side edges of the pile roll up to form these vortices.

These flow effects can introduce extensive scour on an erodible bed in the neighbourhood of the pile and may reduce the stability of pile-supported marine structures such as platforms, bridges, subsea templates, thus leading to their failures. Knowledge of these effects is essential when scour protection around such structures is considered.

In the case of steady currents (wind flows, river flows, etc.) the horseshoe vortex has been investigated quite extensively in the past decades (see Baker 1979; Niederoda & Dalton 1982; Dargahi 1989 for reviews of recent work). Various visualization techniques, such as the smoke technique in a wind tunnel (e.g. Schwind 1962; Baker 1979) and the hydrogen-bubble technique in water (Dargahi 1989), have been used to visualize the horseshoe vortex flow. Also, measurements of pressure and velocity beneath the horseshoe vortex have been carried out (Hjorth 1975; Baker 1979; Dargahi 1989). In Hjorth's and Baker's studies, the distribution of bed shear stress beneath the horseshoe vortex has been calculated from the measured velocity profiles. These latter studies demonstrated that the bed shear stress can be amplified by a factor of 7–11 with respect to its undisturbed value, emphasizing the importance of the horseshoe vortex in scour processes.

On the theoretical side, numerical simulation of the horseshoe-vortex flow has been carried out by several researchers in recent years. Briley & McDonald (1981) made Navier–Stokes computations of a laminar, steady horseshoe vortex at the junction between an elliptic strut and a flat plate at low Mach numbers. Using a three-dimensional incompressible Navier–Stokes code, Kwak *et al.* (1986) computed the laminar, steady junction flow. Deng & Piquet (1992) studied the three-dimensional

turbulent flow about an aerofoil/flat plate junction, capturing the main features of the horseshoe vortex. An iterative, fully decoupled technique was applied to the Reynolds-averaged Navier–Stokes equations in the latter study. A comprehensive review of recent work is given by Deng & Piquet (1992).

Although much effort has been put into the study of horseshoe-vortex flow in the case of steady currents, it appears that no previous study has been conducted to investigate these flows in waves.

Regarding the lee-wake vortex flow, an extensive volume of knowledge has accumulated over the past two decades on the two-dimensional vortex flow behind a free cylinder subject to an oscillatory flow (see e.g. Sarpkaya & Isaacson 1981; Bearman *et al*. 1981; Williamson 1985) and the complex behaviour of vortex motions in various regimes is well understood. However, no study is yet available that investigates these vortex-flow regimes in the case of a pile where the cylinder is confined with a wall at one end.

The purpose of the present investigation is to study in a systematic manner these flow structures, namely the horseshoe and the lee-wake vortices, when the pile is exposed to waves. It turns out that the horseshoe-vortex flow, just as in the case of lee-wake vortex flow, is governed primarily by the Keulegan–Carpenter number, KC. The present work basically focuses on the variations with KC.

2. Experimental set-up

2.1. *Flow-visualization experiments*

These experiments were carried out in a wave flume, 0.6 m in width, 0.8 m in depth and 26.5 m in length. Waves were produced by a piston-type wave generator. The measurement section was located 14 m from the wave generator. In the 11 m long working section of the flume, smooth PVC plates were fixed to the bottom. The water depth was maintained constant at 40 cm throughout the experiments. A honeycomb-type filter was placed in the flume, immediately after the wave generator, to avoid any variation of waves in the transverse direction in the case of waves and to straighten the flow in the case of a steady current.

The hydrogen-bubble technique was used in the experiments to visualize the near-bed flow processes around the junction between the cylinder and the bed. A 25 cm long and 0.050 mm diameter copper wire was used as the hydrogen-bubble wire. It was placed at a right angle to the direction of wave propagation at a streamwise distance of about 1 cm from the edge of the cylinder and at a vertical location of $y = 2$ mm away from the bed. In some of the experiments, a second hydrogen-bubble wire, placed at the opposite side of the cylinder, was used to show the influence of the asymmetry between the wave crest and the wave trough.

Two kinds of piles were used in the experiments. One was a circular cylinder with the diameter $D = 40$ mm and the other was a square-section cylinder of the same width. The surface of the cylinders was smooth. The lowermost 1.2 cm portions of the cylinders were made from a transparent material through which the light was spread, to facilitate flow visualization. The square cylinder was tested for two different orientations to the flow, 90° and 45°, to show the influence of the cross-sectional shape of piles.

The visualized near-bed flow was videotaped. The x-component of the orbital velocity at the point $(x, y, z) = (6, 15, 6)$ cm (figure 1) was recorded simultaneously with the flow visualization as a reference signal. This velocity was measured by a Dantec one-component laser Doppler anemometer (LDA).

Some supplementary tests were made in steady currents and in combined waves and current. The former was for reference, and the latter was for the purpose of studying the influence of a superimposed current on the flow structures observed in the case of waves alone.

2.2. *Bed shear-stress measurements*

These experiments were carried out mainly in the same flume as that used in the flow-visualization experiments. Some supplementary experiments were carried out in a U-shaped oscillatory-flow water tunnel. This tunnel is the same as that described in Jensen, Sumer & Fredsøe (1989). The working section was 10 m long, 0.39 m wide and 0.29 cm high. The top and sidewalls of the working section were made of smooth transparent Perspex plates while the bottom was made of smooth PVC plates.

The same circular cylinder as that used in the flow-visualization tests was used in the flume experiments, while a 5 cm diameter circular cylinder was used in the tunnel experiments. This cylinder was placed vertically in the tunnel, extending the whole tunnel height.

The bed shear stress was measured by a Dantec 55R46 Spec two-component hot-film probe. The probe was mounted flush to the bed. It enabled the magnitude and the direction of the bed shear-stress vector to be measured. Details of the probe and the measurement technique plus the accuracy of the instrument are given in Sumer *et al.* (1993). In some of the flume experiments and in the tunnel experiments the bed shear stress was measured along the principal axes x and y (figure 1). In four tests in the flume experiments (tests 1, 4, 8 and 14, table 1, given in the Appendix), the bed shear stress was measured around the base of the pile in the half-space $y > 0$ over an area extending from $x/D \approx -3$ to $x/D \approx 3$ in the x-direction and from $-y/D = 0$ to $y/D \approx 3.5$ in the y-direction.

The ratio of the flume width to the pile diameter was 15. This figure was about eight in the tunnel experiments. According to the potential flow theory, the blockage effect for these values of the width-to-diameter ratio is less than 1%.

2.3. *Velocity measurements*

The velocities, both the x- and z-components (figure 1), were measured in the plane of symmetry $y = 0$ for $x/D < -0.5$ using the previously mentioned LDA equipment. Also, the velocity profile measurements were carried out in the case of undisturbed-flow situations, using the same LDA equipment.

3. Test conditions

Tables 1–4 in the Appendix summarize the test conditions. T is the wave period or the period of the oscillatory flow. U_m is the maximum value of the undisturbed orbital velocity at the bed in the case of waves (the flume experiments) and that of the free-stream velocity in the case of oscillatory flow (the tunnel experiments). V_0 is the undisturbed free-stream velocity in the case of steady current, and U_c is the velocity of the current component of the undisturbed combined flow, measured at the edge of the wave boundary layer (see the small box for the definition sketch in figure 10; $u = U_m$ at $z = \delta_1$). The quantity a is the amplitude of the undisturbed oscillatory flow,

$$a = \frac{U_m T}{2\pi}. \tag{1}$$

U_{fm} is the maximum value of the friction velocity in the case of waves and oscillatory flow, defined by

$$U_{fm} = (\bar{\tau}_{0m}/\rho)^{1/2} \tag{2}$$

in which $\bar{\tau}_{0m}$ is the maximum value of the undisturbed bed shear stress, and U_f is the friction velocity in the case of a steady current:

$$U_f = (\bar{\tau}_{0\infty}/\rho)^{1/2} \tag{3}$$

in which $\bar{\tau}_{0\infty}$ is the undisturbed bed shear stress. The overbar in the above equations and throughout the paper denotes ensemble averaging in the case of waves and oscillatory flow, and time averaging in the case of steady current. *Re* is the Reynolds number of the undisturbed wave boundary layer defined by

$$Re = aU_m/\nu \tag{4}$$

in which ν is the kinematic viscosity. δ is the thickness of the undisturbed boundary layer; in the case of waves and oscillatory flow it is defined such that

$$u = u_{max} \quad \text{at} \quad z = \delta \quad \text{and} \quad \omega t = 90° \tag{5}$$

(Jensen *et al*. 1989, figure 24).

For the experiments where the flow is laminar, namely all the wave tests and the first three tunnel tests (tables 1 and 4), δ values are obtained from the familiar laminar boundary-layer solution (Batchelor 1967, p. 354) that can be expressed as

$$\frac{\delta}{a} = \frac{3\pi}{4}\left(\frac{2}{Re}\right)^{1/2}. \tag{6}$$

For the experiments where the flow is transitional (tests 66 and 67), δ values are calculated from the experimental information given in Jensen *et al*. (1989). In the case of steady current (tests 48–51), δ is taken as the entire flow depth.

The quantity *KC* in the table is the Keulegan–Carpenter number, defined by

$$KC = U_m T/D. \tag{7}$$

Re_δ and Re_D are the boundary-layer-thickness Reynolds number and the pile Reynolds number, respectively, defined by

$$Re_\delta = \begin{cases} \delta U_m/\nu & \text{for waves/oscillatory flow} \\ \delta V_0/\nu & \text{for steady current,} \end{cases} \tag{8}$$

and

$$Re_D = \begin{cases} DU_m/\nu & \text{for waves/oscillatory flow} \\ DV_0/\nu & \text{for steady current.} \end{cases} \tag{9}$$

4. Undisturbed flow

4.1. *Wave experiments*

The undisturbed flow was measured in four different characteristic wave regimes (tests 1, 4, 8 and 14). Figure 2 depicts time series of the outer flow velocity U_0, measured at $z = 5$ cm. As seen, the signal diverges from a sinusoidal variation for the last three cases. This is because of the large wave heights and wave periods, required to achieve large *KC*.

As seen from table 1, the wave boundary-layer Reynolds number, *Re*, is always

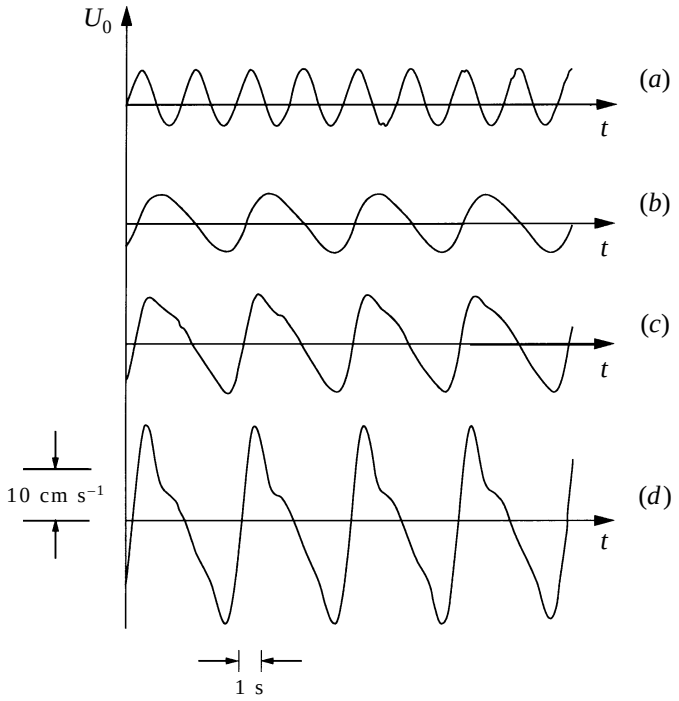

FIGURE 2. Time series of the undisturbed free-stream velocity U_0 measured at $z = 5$ cm at the measurement section. (*a*) H (the wave height) = 2.4 cm, $T = 2.2$ s, $U_m = 5.1$ cm s^{-1} (test 1); (*b*) $H = 2.3$ cm, $T = 4.4$ s, $U_m = 5.5$ cm s^{-1} (test 4); (*c*) $H = 3.9$ cm, $T = 4.4$ s, $U_m = 9.4$ cm s^{-1} (test 8); (*d*) $H = 8.0$ cm, $T = 4.4$ s, $U_m = 18.3$ cm s^{-1} (test 14).

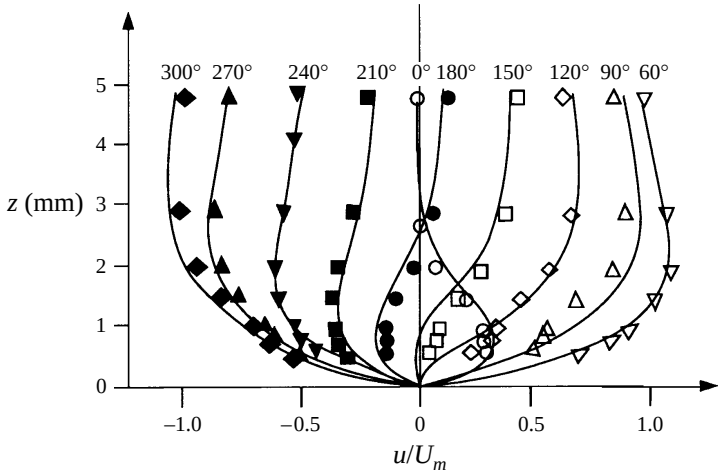

FIGURE 3. Undisturbed velocity profiles at the measurement section; waves alone, test 14. Symbols: measured profile; solid lines: laminar flow solution.

smaller than the critical Reynolds number, $Re_{cr} \approx 1.5 \times 10^5$ (Sleath 1984), indicating that the wave boundary layer in the experiments was laminar.

Figure 3 gives the undisturbed flow velocity profiles measured in test 14, together with the laminar-flow-solution profiles (the solid lines). The laminar solution profiles

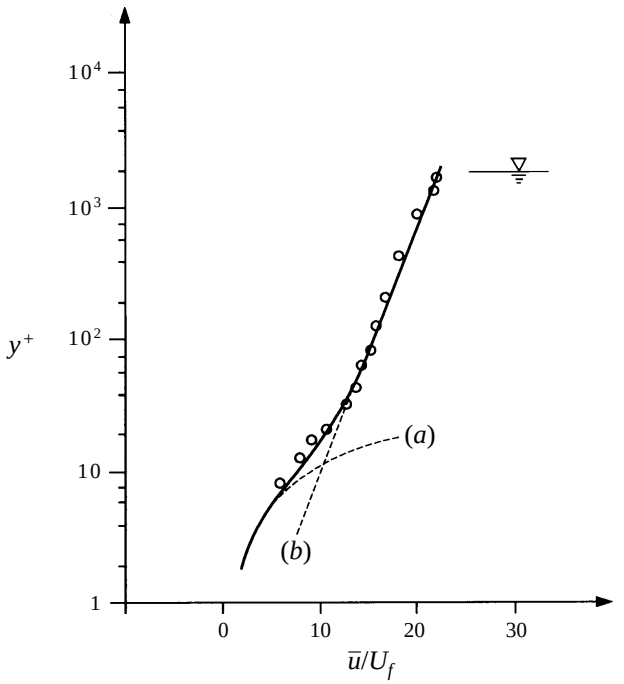

FIGURE 4. Undisturbed velocity profile at the measurement section; steady current. Symbols, measured profile; solid line, the van Driest profile; dashed lines, (*a*) $\bar{u}/U_f = y^+$ and (*b*) $\bar{u}/U_f = (1/\kappa)\ln y^+ + 5$.

are obtained for the orbital velocity variation measured in the test, which is approximated by

$$\frac{u_0}{U_m} = a\sin(\omega t) + b\sin(2\omega t), \tag{10}$$

and the solution is obtained by superposition of two laminar solutions, one for the velocity variation represented by the first term and the other for the next term on the right-hand side of (10). Here ω is the angular frequency, and a and b are coefficients determined by the least-square method. Figure 3 shows that the agreement between the measurements and the laminar solution is good.

4.2. *Current experiments*

Figure 4 depicts the measured undisturbed velocity profile together with the van Driest (1956) profile,

$$\frac{\bar{u}}{U_f} = 2\int_0^{y^+} \frac{\mathrm{d}y^+}{1+\{1+4\kappa^2 y^{+^2}[1-\exp(-y^+/A)]^2\}^{1/2}}, \tag{11}$$

in which $y^+ = yU_f/\nu$, κ is the Kármán constant (taken as $\kappa = 0.42$) and A is the van Driest damping factor ($= 25$). The friction velocity, obtained by fitting the van Driest profile to the measured velocity profile, is $U_f = 0.42\ \mathrm{cm\ s^{-1}}$. This value agrees well (within about 10 %) with the value measured by the hot-film probe referred to in §2.2 (see table 2).

No velocity profile measurements were made in the case of combined waves and current tests (tests 52–62). The flow velocity traces (obtained by the LDA measurements) indicated that the flow in these experiments was in the turbulent regime.

4.3. *Oscillatory-flow experiments*

From the extensive boundary-layer measurements carried out in the same oscillatory-flow tunnel (Jensen *et al.* 1989) it was concluded that (i) for tests 63–65 the undisturbed boundary layer was the in laminar regime and represented quite well by the laminar sinusoidal oscillatory flow solution (Batchelor 1967, p. 354), and (ii) for the other tests (tests 66 and 67), it was in the transitional flow regime. The velocity profiles for the latter case are presented in Jensen *et al.* (1989).

5. Horseshoe vortex

5.1. *KC dependence*

The near-bed flow around a pile partly consists of the horseshoe vortex (formed at the bed in front of the pile) and partly of the vortex flow pattern (formed at the lee side of the pile) (figure 1), as mentioned previously.

The horseshoe vortex is formed at the bed because of the rotation in the incoming flow velocity (figure 1). In waves, this rotation occurs in the wave boundary layer.

The non-dimensional quantities describing the horseshoe vortex in the case of a steady current depend mainly on the following parameters (Baker 1979):

$$Re_D, \quad \delta/D, \quad \text{pile geometry.} \tag{12}$$

In the case where the pile is exposed to waves, an additional parameter, the Keulegan–Carpenter number, KC (equation (7)), emerges. From (7), KC is proportional to the ratio $2a/D$, where $2a$ represents the stroke of the motion at the bed (figure 1). Small KC therefore means that the orbital motion of water particles is small relative to the width of the pile. When KC is very small, the horseshoe vortex may not even be formed, because the stroke of the motion is not large enough for the incoming boundary layer to separate. For very large KC, on the other hand, the stroke of the motion is so large that the flow in each half-period resembles that in steady currents. Therefore, the horseshoe vortex may be expected to behave in much the same way as in the case of a steady current.

The preceding considerations imply that the formation and development of the horseshoe vortex in the case of waves is heavily influenced by KC.

5.2. *The existence of a horseshoe vortex*

Figure 5 depicts the flow in front of the base of the pile for two KC: 2.8 and 10.3. The sharp, crescent shape (A) in the pictures represents the lowermost transparent portion of the pile through which the light spreads out. The horseshoe vortex manifests itself in the photographs by the absence of the bubbles in the immediate surroundings of the pile (figure 5*b* where $KC = 10.3$), while the presence of the bubbles in the immediate surroundings of the pile means that there is no horseshoe vortex (figure 5*a* where $KC = 2.8$). The vector diagram presented in figure 6 further reveals the existence of the horseshoe vortex for the same conditions as in figure 5(*b*) (for $KC = 10.3$).

The results of the present flow visualization analysis together with the analysis of the bed shear stress data are plotted in figure 7. In the flow visualization analysis, the small time resolution of video (namely, 1/25 s) and the small incremental increase of KC enabled us to detect rather accurately the onset of a horseshoe vortex (i.e. the limit to the existence of horseshoe vortex) as a function of KC, plotted in figure 7. In the bed shear stress analysis, the presence of the horseshoe vortex was detected from the direction of the bed shear stress vector.

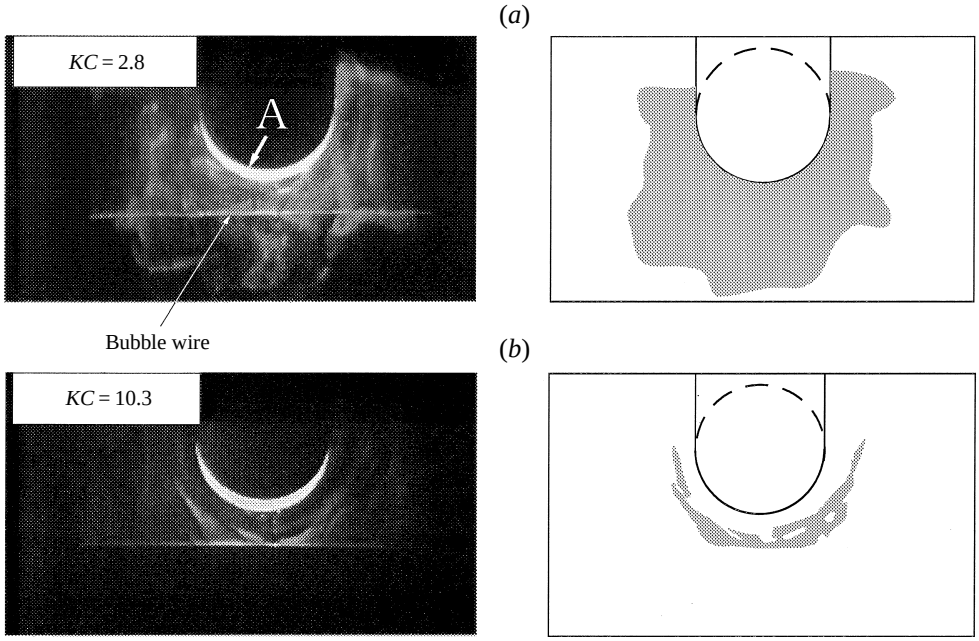

FIGURE 5. Picture of the flow in front of the base of circular pile. A: lowermost portion of the pile (made of transparent material) through which light spreads out. There is no horseshoe vortex for (*a*), but there is one for (*b*). $\omega t = 100°$ in (*a*) and 90° in (*b*).

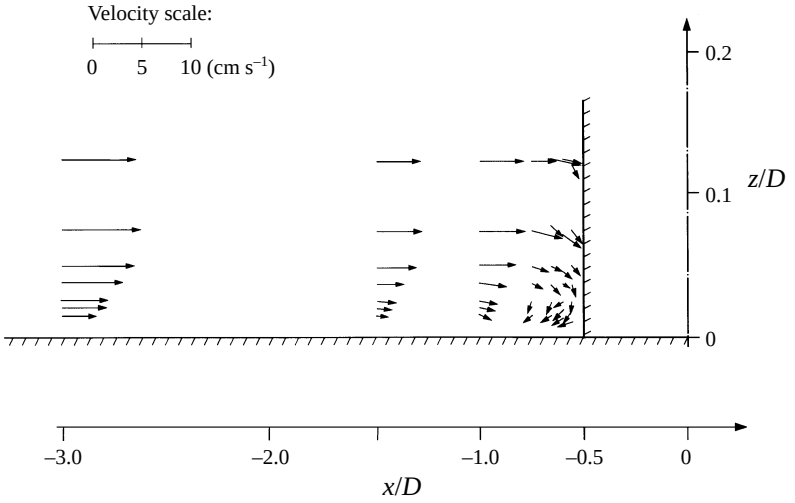

FIGURE 6. Vector diagram illustrating the horseshoe vortex in the $y = 0$ plane. $KC = 10.3$ and $\omega t = 90°$.

Figure 7 indicates that (i) no horseshoe vortex exists for KC below 6, and (ii) the horseshoe vortex first emerges when $KC = 6$ and is maintained over a larger and larger span of ωt, as KC is increased. (The asymmetry observed in figure 7 between the two half-periods is due to the asymmetry in the waves (figure 2).)

For the Re_D experienced in the present tests ($Re_D = O(10^3)$), the flow over the pile surface separates at about $KC = 1$ (see Sarpkaya 1986), whereas the present results

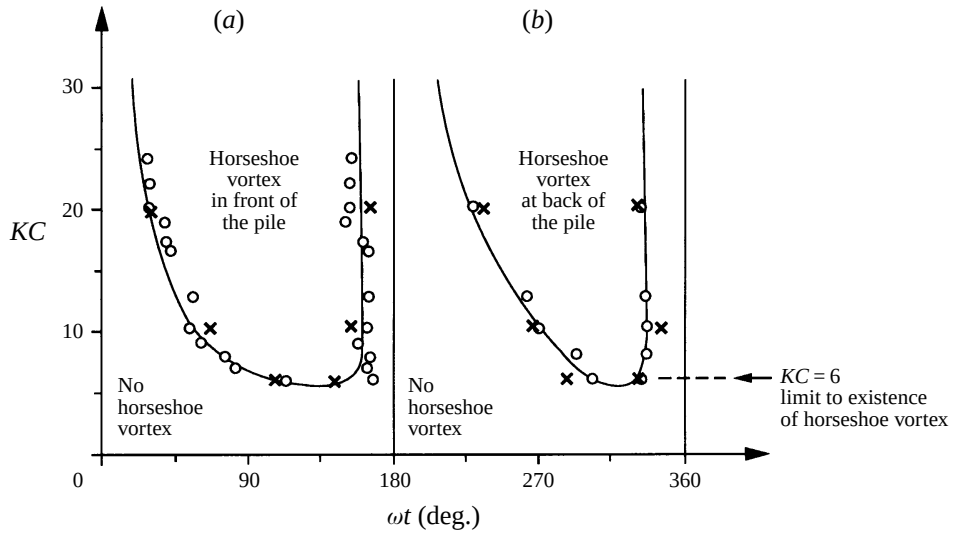

FIGURE 7. Occurrence of horseshoe vortices in phase space, circular pile. Circles, from the flow-visualization experiments; crosses, from the bed shear stress measurements.

show that the flow in front of the pile separates at $KC = 6$, a much higher KC than that needed for the flow separation at the pile surface. The question is then: what mechanism suppresses the boundary-layer separation in front of the pile for KC below 6? This is related to the adverse pressure gradient. Using potential-flow theory, the pressure gradient in front of the pile (along the x-axis) can be written as

$$\frac{\partial p}{\partial x} = \frac{1}{2}\frac{\rho U_\infty^2}{D}\left[1 - \frac{1}{4(x/D)^2}\right]\left[\frac{1}{(x/D)^3}\right]. \tag{13}$$

Likewise, the pressure gradient over the surface of the pile, again using potential-flow theory, can be written as

$$\frac{\partial p}{\partial x'} = -8\frac{\rho U_\infty^2}{D}\sin(2x'/D)\cos(2x'/D), \tag{14}$$

in which x' is the distance along the pile surface measured from the stagnation point (i.e. from the point $x = -0.5D$, $y = 0$). From (13) and (14), it is found that the maximum value of the adverse pressure gradient in front of the pile is a factor 5 smaller than that over the surface of the pile. This explains why the separation is 'delayed' in front of the pile until after KC reaches the value of 6, a considerably larger value than that necessary for the flow separation over the pile surface (namely, $KC = 1$).

Figure 8 presents a sequence of pictures illustrating the development of the horseshoe vortex during the course of approximately one half-period of the waves for $KC = 10.3$. The horseshoe vortex first emerges only after ωt reaches about 50° (frame 2). It grows in size as the flow develops (frames 3 and 4), and eventually gets disrupted by the leewake, which is washed around the pile just prior to the flow reversal (frame 5), and presumably it then disappears.

Figure 8 (frames 3 and 4) shows that there are some secondary horseshoe vortex formations (a in frame 3 and b and c in frame 4). This indicates that the main vortex causes the boundary layer to separate into a series of secondary vortices, known from

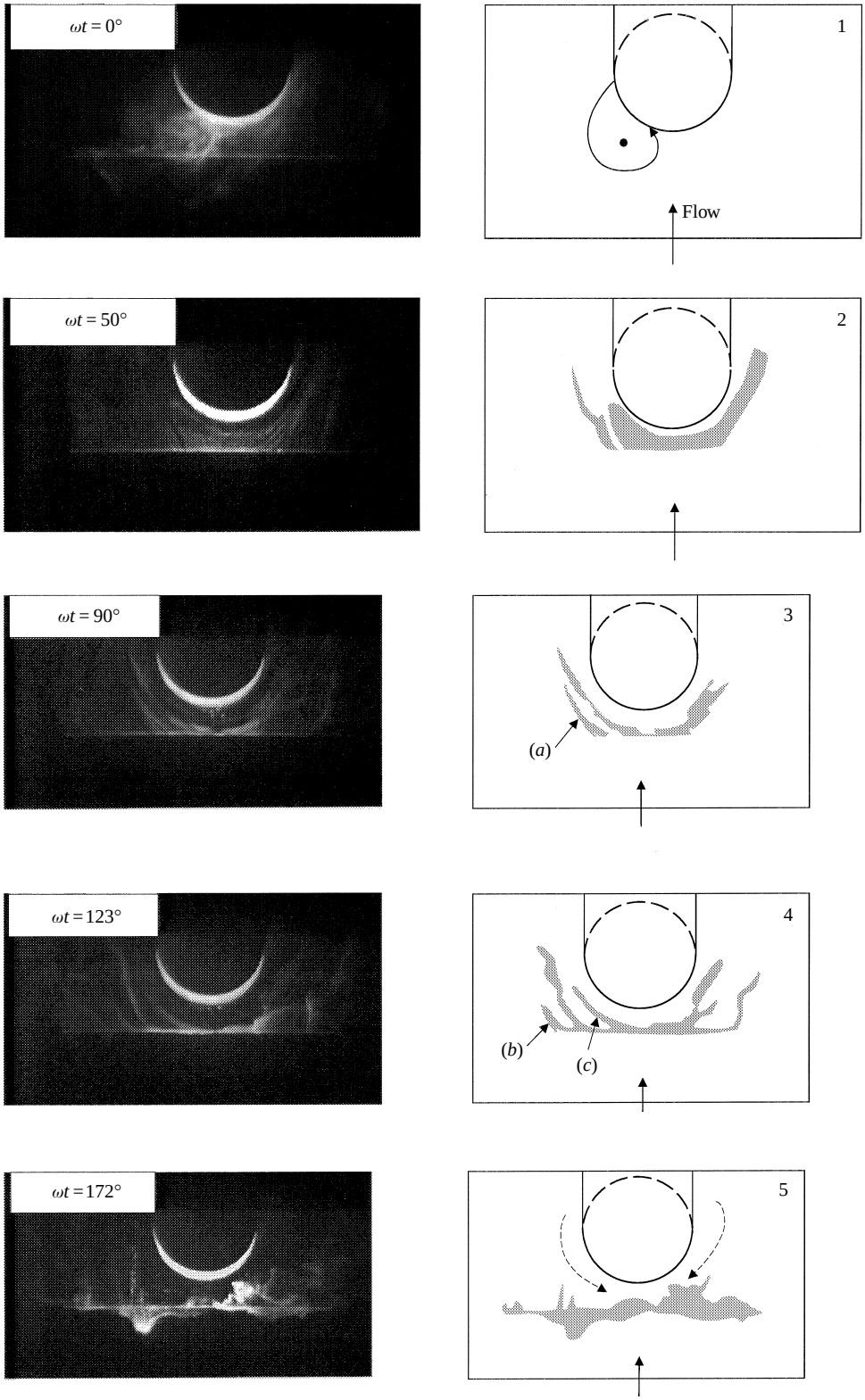

FIGURE 8. Time evolution of the horseshoe vortex in waves; circular pile. $KC = 10.3$.

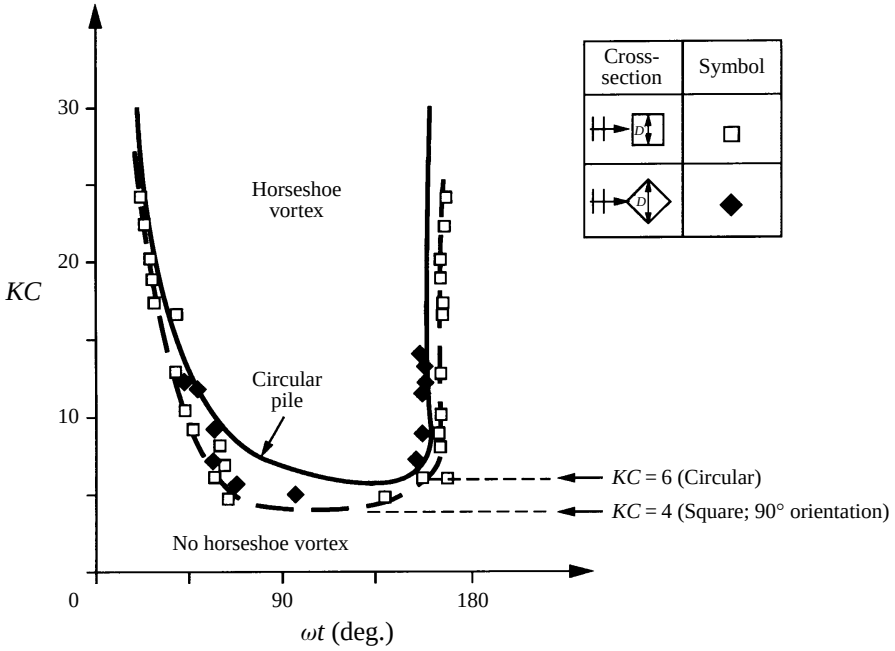

FIGURE 9. Presence of horseshoe vortex in phase space: influence of cross-sectional shape. Crest half-period ($\omega t = 0°$–$180°$). The circular-pile curve is from figure 7.

the steady-current horseshoe-vortex research (e.g. Baker 1979 and Dargahi 1989). It was observed that these smaller-scale vortices were rather turbulent and impermanent.

5.2.1. *Influence of cross-section*

Figure 9 displays the results of the square-section-pile flow-visualization experiments together with the circular-pile ones (figure 7*a*), illustrating the influence of cross-section on the formation of the horseshoe vortex in phase space. Comparison is made only for the crest half-period, $\omega t = 0°$–$180°$. The horseshoe vortex appears at a slightly lower KC in the case of the square-section pile with 90° orientation, namely at $KC = 4$, than in the case of the circular pile. This obviously leads to larger lifespans (§5.3). The reason why the flow separates (and therefore the horseshoe vortex comes into existence) at a smaller KC is that the adverse pressure gradient generated in front of the square-section pile is larger than that generated in front of the circular pile.

As regards the square pile with 45° orientation, the critical KC beyond which the horseshoe vortex exists apparently lies between 4 and 6.

5.2.2. *Influence of superimposed current*

Figure 10 illustrates the influence of a superimposed current on the horseshoe vortex. Only the data corresponding to the half-period where the waves are propagating in the same direction as the current ($\omega t = 0°$–$180°$) are shown. It is clear that the horseshoe vortex exists for smaller and smaller KC with increasing U_c/U_m. This result is directly related to the increase in the adverse pressure gradient in front of the pile caused by the superimposed current. The larger the value of the current-to-wave velocity ratio, U_c/U_m, the larger the adverse pressure gradient in front of the pile, therefore the more favourable the flow environment for the horseshoe vortex to be formed.

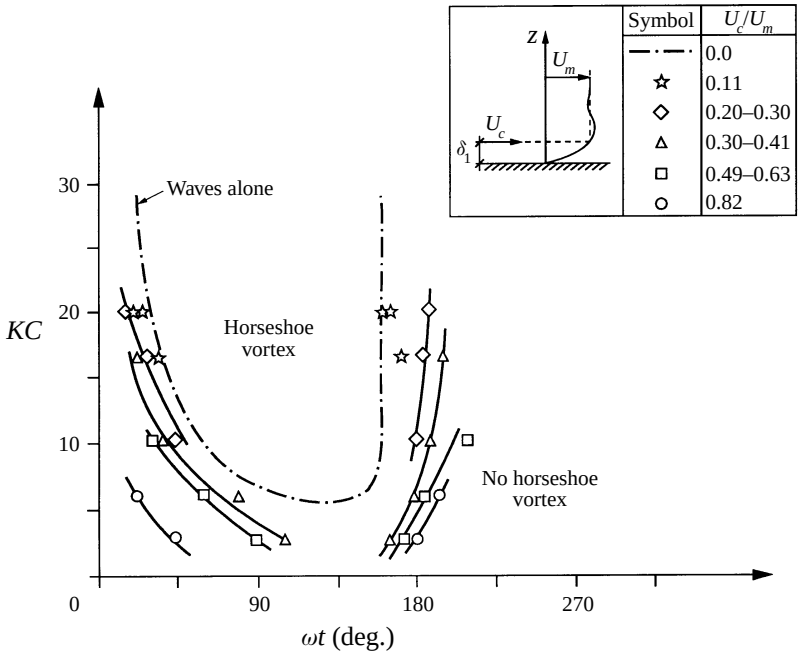

FIGURE 10. Presence of horseshoe vortex in phase space: influence of superimposed current. Circular pile. The half-period where the current is in the same direction as that of wave propagation. Waves-alone curve is from figure 7.

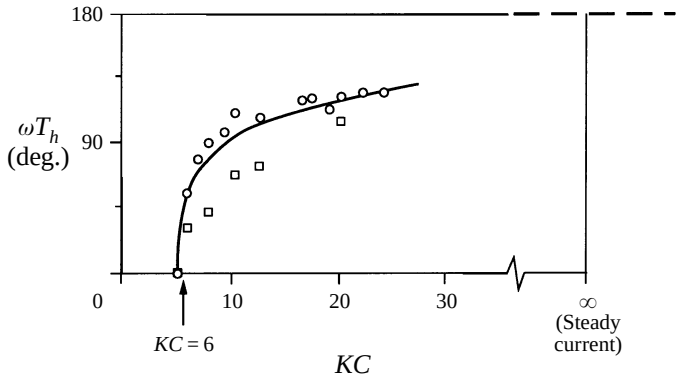

FIGURE 11. Lifespan of horseshoe vortex; circular pile. Circles, for the horseshoe vortex formed in front of the pile; squares, for that formed behind the pile.

5.3. *Lifespan of a horseshoe vortex*

Figure 11 presents the circular-cylinder data related to the lifespan of the horseshoe vortex, T_h, as function of KC, obtained from figure 7. T_h here is defined by

$$\omega T_h = (\omega t)_2 - (\omega t)_1, \tag{15}$$

in which $(\omega t)_1$ is the phase at which the separation occurs and therefore the horseshoe vortex appears, and $(\omega t)_2$ is the phase at which the horseshoe vortex completely disappears. The circular symbols correspond to the horseshoe vortex being formed in

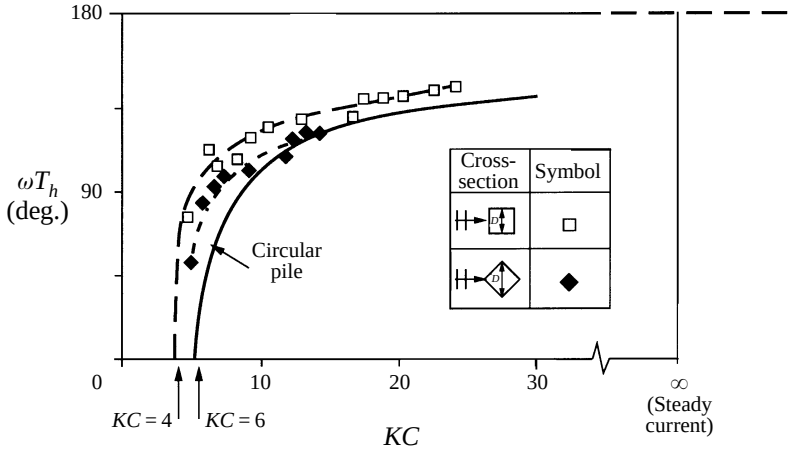

FIGURE 12. Lifespan of horseshoe vortex: influence of cross-sectional shape. Circular-pile curve is from figure 11.

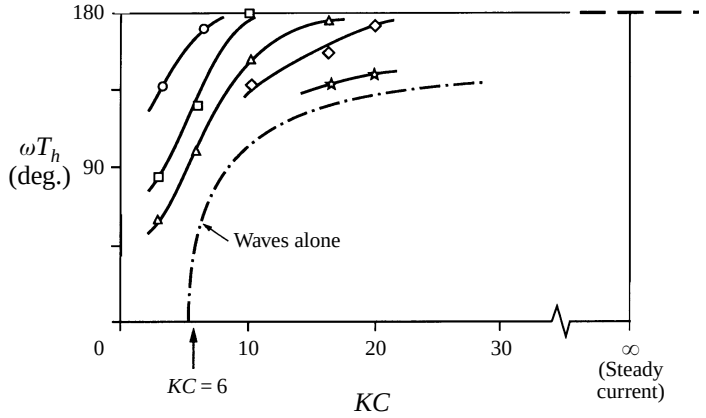

FIGURE 13. Lifespan of horseshoe vortex: influence of superimposed current. Circular pile. The half-period where the current is in the same direction as that of wave propagation. Symbols are the same as in figure 10. Waves-alone curve is from figure 11.

front of the pile while the square ones correspond to that behind the pile. The difference between the two is due to asymmetry in the waves, as mentioned above.

Figure 12 shows the influence of cross-sectional shape on the lifespan of a horseshoe vortex. (Comparison is made only for the crest half-period, $\omega t = 0°$–$180°$). As seen in the preceding subsection, the horseshoe vortex appears at a smaller KC, namely at $KC = 4$, in the case of the square pile with 90° orientation than in the case of the circular pile (figure 9). This implies that the lifespan of a horseshoe vortex must be larger in the former case than in the latter case, as revealed by figure 12. The figure further shows that the result for the square-section pile with 45° orientation lies between the circular pile and the 90°-orientation square pile.

The influence of current on the lifespan of a horseshoe vortex is depicted in figure 13. (Only the data corresponding to the half-period where the waves are propagating in the same direction as the current, $\omega t = 0°$–$180°$, are shown). The lifespan of the horseshoe vortex in phase space is increased quite substantially with increasing U_c/U_m.

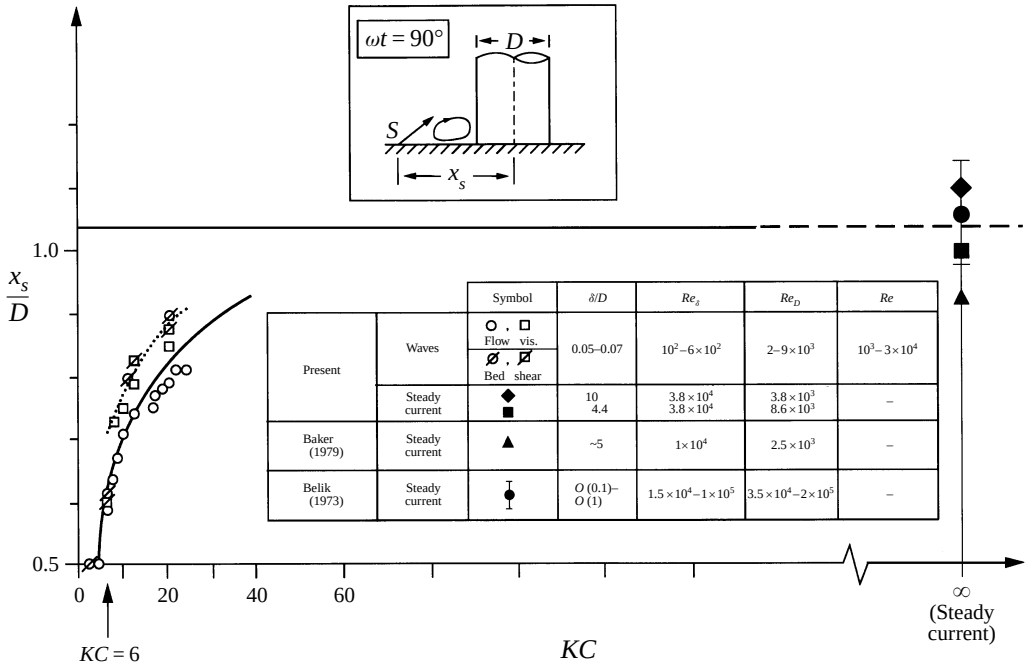

FIGURE 14. Separation distance; circular pile. Circles, for the horseshoe vortex formed in front of the pile ($\omega t = 90°$); squares, for that formed behind the pile ($\omega t = 270°$); open symbols, the incoming boundary layer is laminar; filled symbols, the incoming boundary layer is turbulent; dotted line, from Baker's (1985) empirical expression (equation (16)).

This is due to the increase in the adverse pressure gradient in front of the pile with increasing current.

5.4. *Separation position*

Figure 14 depicts the separation distance, x_s, associated with the formation of the horseshoe vortex (see also figure 1). x_s is measured from the centre of the pile. The plotted data correspond to the phase values $\omega t = 90°$ and 270° (the circles and squares, respectively). The x_s values were obtained both from the flow visualization films and from the bed shear stress measurements. The figure also includes the steady current results of the present study as well as the results from the studies of Belik (1973) and Baker (1979) plus Baker's (1985) empirical expression (see below). From figure 14, x_s first experiences a steep increase with KC, and then it tends to approach its asymptotic value (the steady-current value), $KC \to \infty$. From figure 14, the x_s values obtained from the bed shear stress measurements appear to be slightly larger than those obtained from the flow visualization study. This is because the latter does not enable the separation point to be detected precisely; in fact, the upstream edge of the visualized hydrogen-bubble band lies a little downstream of the actual separation line.

Figure 14 includes Baker's (1985) empirical expression for laminar horseshoe systems, with zero pressure gradient in steady currents:

$$x_s/D = 0.5 + 0.3(Re_D)^{0.48}(\delta^*/D)^{0.96} \tanh(3h/D), \tag{16}$$

in which δ^* is the displacement thickness of the undisturbed boundary layer and h is the pile height. Since, at the phase values $\omega t = 90°$ and 270°, the undisturbed pressure gradient is zero, we may compare the present results plotted in figure 14 with the Baker

	Cross-section	Symbol	δ/D	Re_δ	Re
Waves	Circular	———	0.05–0.07	$10^2-6\times10^2$	$10^3-3\times10^4$
	45°, square	◇	0.04–0.05	$10^2-6\times10^2$	$10^3-3\times10^4$
	90°, square	□	0.05–0.07	$10^2-6\times10^2$	$10^3-3\times10^4$
Steady C.	Circular	●	10	3.8×10^4	–
	45°, square	◆	7	3.8×10^4	–
	90°, square	■	10	3.8×10^4	–

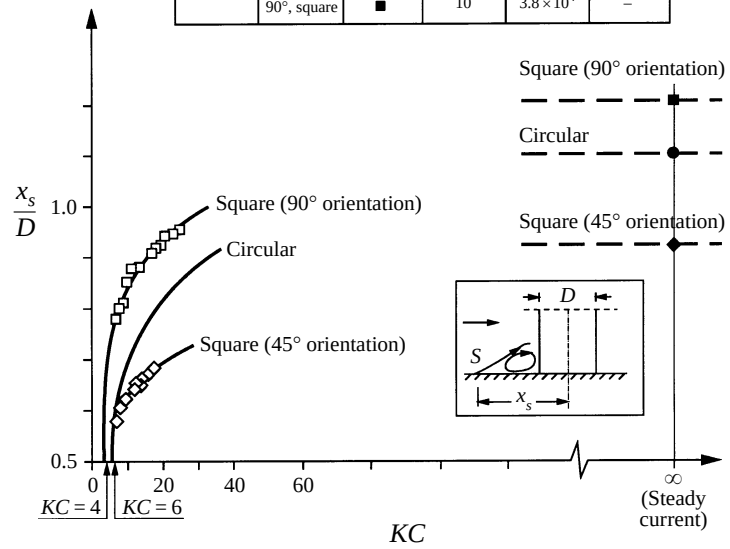

FIGURE 15. Separation distance at $\omega t = 90°$: influence of cross-sectional shape. Circular-pile curve is from figure 14. Open symbols: the incoming boundary layer is laminar; filled symbols: the incoming boundary layer is turbulent.

formula (16). For this, δ^* is predicted using the relationship $\delta^* = (2/3\pi)\,\delta$, obtained from the laminar-flow oscillatory boundary-layer solution (Batchelor 1967, p. 192), corresponding to the present tests. Also, $h/D \to \infty$ in the present tests. From the figure, there appears to be a reasonable agreement between the present results and that predicted by the Baker formula.

Finally, the scatter in the data for $KC = \infty$ (the steady-current case) in figure 14 is due to the Reynolds number effect; an inspection of the data indicates that x_s/D increases with increasing Re_D, in agreement with the results of Baker (1979).

Figure 15 shows the influence of cross-sectional shape on the separation position associated with the horseshoe vortex. (Comparison is made only for the crest half-period, $\omega t = 0°$–$180°$.) The figure shows that, for a given KC, x_s/D is largest for the square pile with 90° orientation and smallest for the square pile with 45° orientation, the circular pile result being in between. This is linked to the streamwise extent of the adverse pressure gradient induced by the pile, which is largest for the square pile with 90° orientation, moderate for the circular pile and smallest for the square pile with 45° orientation.

Figure 16 shows the influence of superimposed current on the position of the separation point. (Only the data corresponding to the half-period where the waves are propagating in the same direction as the current, $\omega t = 0°$–$180°$, are depicted.) As seen, x_s/D increases quite markedly with increasing values of U_c/U_m. This is again directly

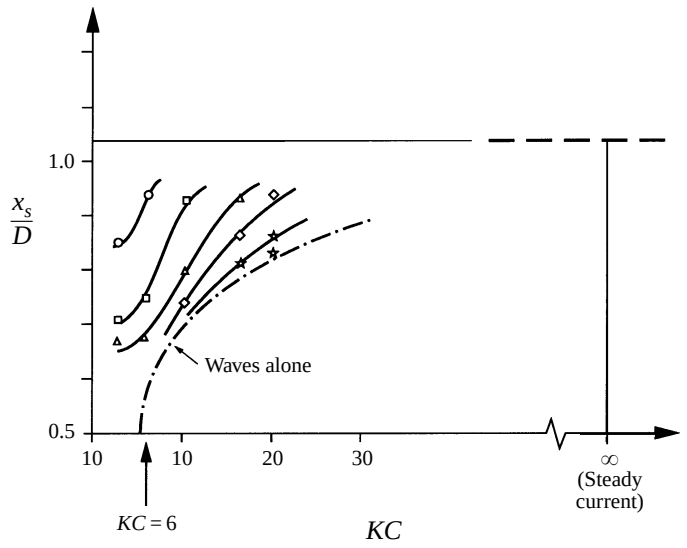

FIGURE 16. Separation distance at $\omega t = 90°$: influence of superimposed current. Circular pile. The half-period where the current is in the same direction as that of wave propagation. Symbols are the same as in figure 10. Waves-alone curve and the asymptote (dashed line) as $KC \to \infty$ are from figure 14.

related to the increase in the adverse pressure gradient in front of the pile caused by the superimposed current, as pointed out in § 5.2. The larger the value of the current-to-wave velocity ratio, U_c/U_m, the larger the adverse pressure gradient in front of the pile, therefore the more pronounced the horseshoe vortex.

5.5. *Bed shear stress beneath the horseshoe vortex*

Figure 17 shows the variation of the bed shear stress along the x-axis (figure 1) at the phase values $\omega t = 90°$ and 270°. When $\omega t = 90°$, the wave-induced flow is from left to right, (called the crest half-period) and the horseshoe vortex is formed in front of the pile, while when $\omega t = 270°$, the flow is from right to left (called the trough half-period) and the horseshoe vortex is formed at the back of the pile. The steady current results together with Baker's (1979) data are also included in the figure. The small asymmetry in the bed shear stress distributions with respect to x is due to asymmetry in the waves (figure 2*b*, *c*, *d*). Figure 17(*a*) ($KC = 2.8$) shows that no horseshoe vortex exists for $\omega t = 90°$ and 270°, as no negative bed shear stress is measured for this KC. The measurements showed that this was the case for all ωt values, revealing that no horseshoe vortex is formed for $KC = 2.8$, in agreement with the visual observations (figures 5*a*, 7, 11 and 14).

Figure 17(*b*–*e*) illustrates quite clearly the increase in the streamwise extent of the horseshoe vortex (the bed area where $\bar{\tau}_0 < 0$) with KC (cf. figure 14).

The bed shear stress under the horseshoe vortex at a distance $0.1D$ from the upstream edge of the base of the pile is plotted in figure 18 together with the results of the present oscillatory water tunnel experiments. Figure 18 shows that the bed shear stress under the horseshoe vortex increases with increasing KC. This is a direct result of the increased presence of the horseshoe vortex with increasing KC (figures 11, 14 and 17).

The scatter in the data for $KC = \infty$ (the steady-current case) in figure 18 is due to the Reynolds number effect. As mentioned previously in conjunction with figure 14, the

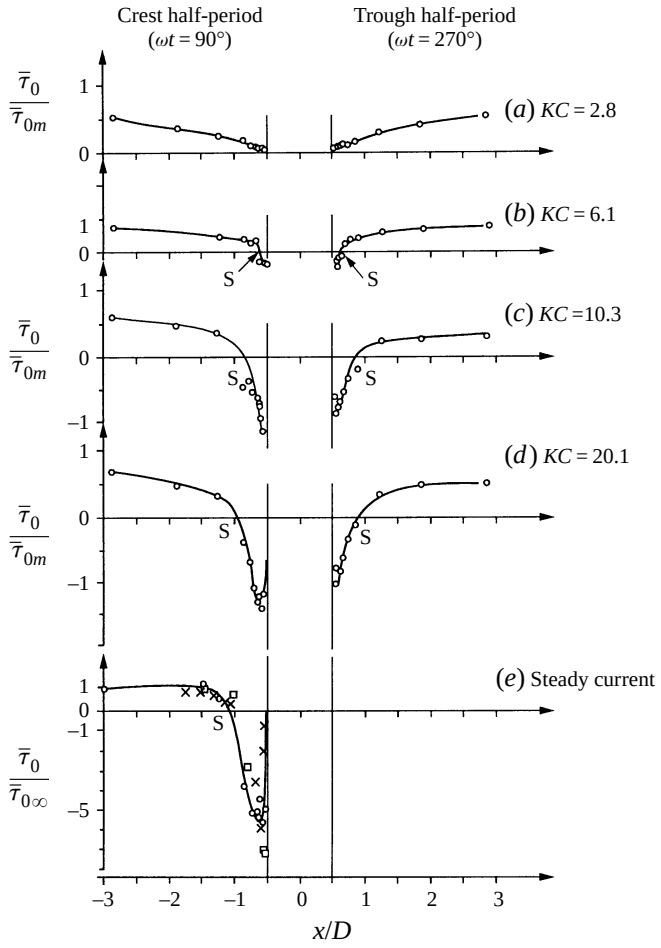

FIGURE 17. Bed shear stress along the x-direction at the horseshoe vortex side of the pile. Circular pile. S = Separation point. Symbols: circles, present results (tests 1, 4, 8, 14 and 48); squares, present results (test 49); crosses, Baker's (1979) air experiments, where $D = 7.6$ cm, $V = 51$ cm s^{-1}, $D/\delta^* = 14.8$ and $Re_D = 2610$, δ^* being the undisturbed displacement thickness of the boundary layer.

larger the Reynolds number, Re_D, the larger the separation distance x_s, therefore the larger the bed shear stress under the horseshoe vortex. The steady-current data in figure 18 appear to reveal this.

Figure 19 depicts the root-mean-square (r.m.s.) value of the fluctuating component of the bed shear stress under the horseshoe vortex (at a distance $0.1D$ from the upstream edge of the cylinder), plotted against KC. First, a non-zero r.m.s. value means that the horseshoe vortex is not in the laminar regime. Figure 19 indicates that, while the horseshoe vortex is in the turbulent regime for $KC = 20$ and ∞ (the steady-current case), it is in the laminar regime for $KC = 6$ (for both half-periods of the waves) and for $KC = 10$ (for only the trough half-period). From the figure it is inferred that the transition to turbulence in the horseshoe vortex begins to occur somewhere between $KC = 10$ and 20. (Recall that the incoming wave boundary layer for these KC, and indeed for all the other KC in the present flume experiments, was in the laminar regime (tables 1–3.)

Now, Baker's (1991) work on the oscillation of horseshoe-vortex systems in steady

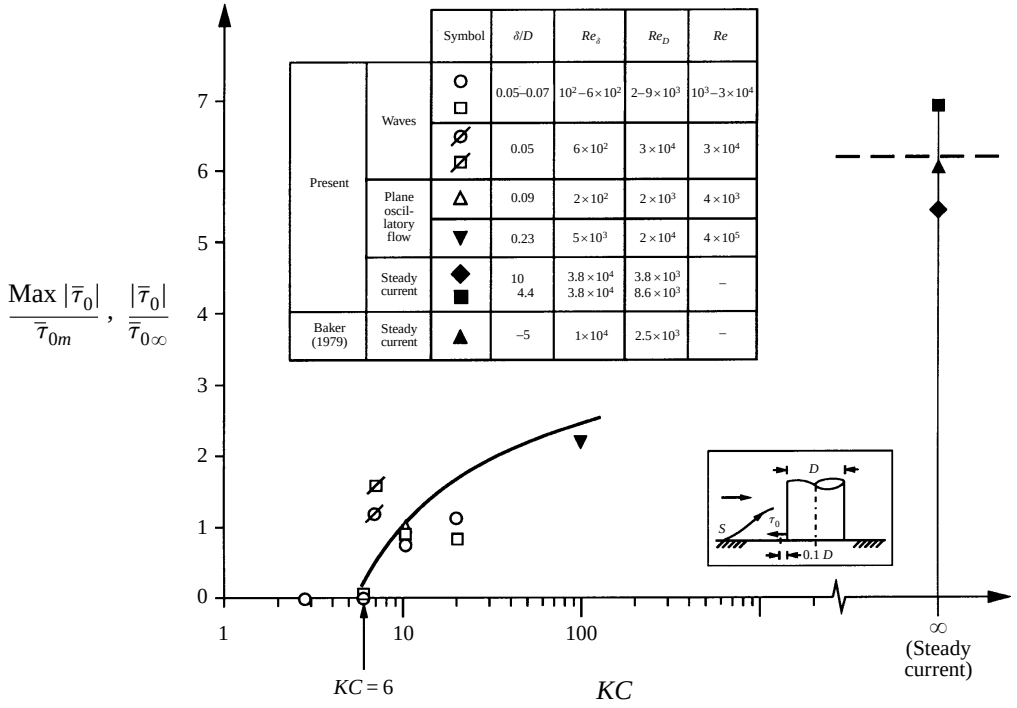

FIGURE 18. Amplification in the bed shear stress beneath the horseshoe vortex at $0.1D$ distance from the upstream edge of the base of the pile; circular pile. Symbols: circles, for the horseshoe vortex formed in front of the pile; squares, for that formed behind the pile; open symbols, the incoming boundary layer is laminar; filled symbols, the incoming boundary layer is turbulent.

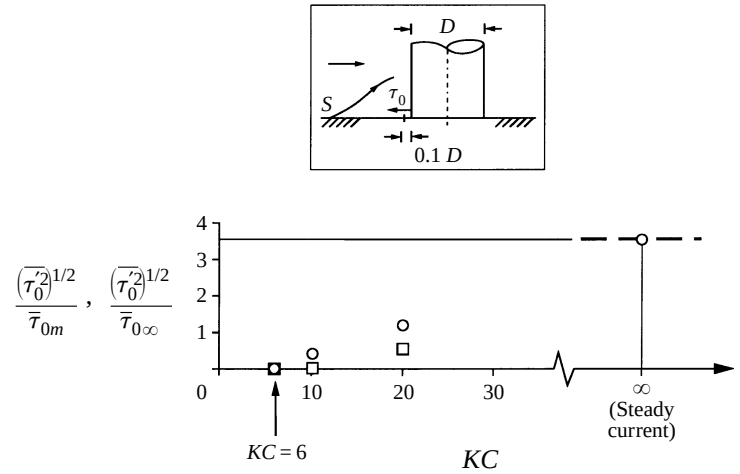

FIGURE 19. The r.m.s. value of the fluctuating component of the bed shear stress under the horseshoe vortex; circular pile. Circles, in front of the pile (at $\omega t = 90°$); squares, behind the pile (at $\omega t = 270°$).

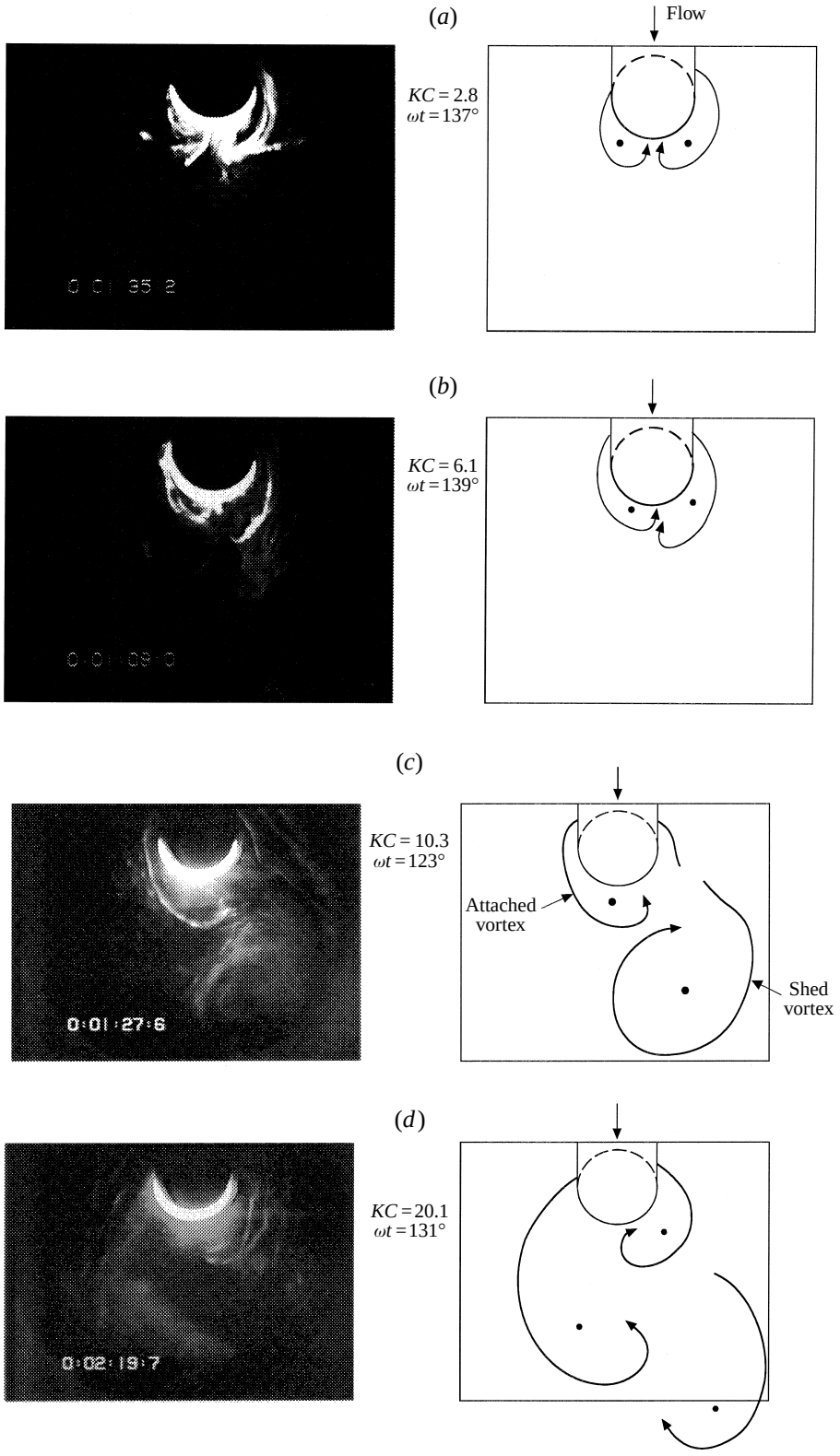

FIGURE 20. The structure of the near-bed wake vortices illustrated for different *KC*.

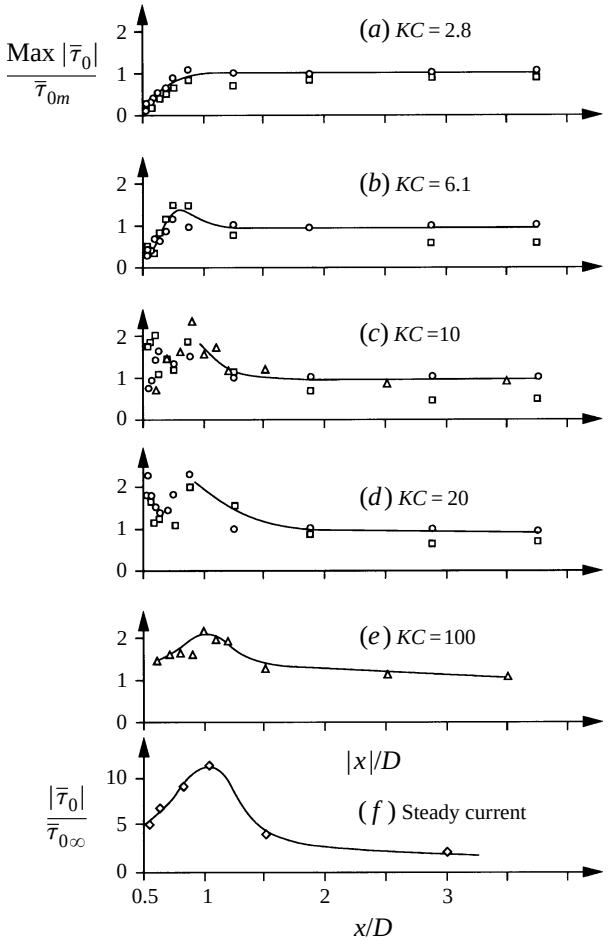

FIGURE 21. Amplification of the bed shear stress along the x-axis at the lee-side of a pile. Circular pile. Circles, in front of the pile; squares, behind the pile; triangles, the oscillatory-tunnel experiments.

currents shows that the so-called primary oscillations (the oscillations of the separated flow system) first emerge when (Baker 1991, figure 3).

$$Re_D(\delta^*/D)^{1/2} = 800, \tag{17}$$

while the so-called secondary oscillations (those of the vortex core) first emerge when (Baker 1991, figure 5)

$$Re_{\delta^*} = 150. \tag{18}$$

It should be emphasized that these limits define the boundaries of the flow regimes where the separated flow system and the horseshoe vortex become of oscillatory character, but not truly turbulent.

The preceding non-dimensional quantities corresponding to the transition observed in the present tests (i.e. that occurring at $KC = 10$–20), are found to be

$$Re_D(\delta^*/D)^{1/2} = 500\text{–}900 \tag{19}$$

and

$$Re_{\delta^*} = 60\text{–}110, \tag{20}$$

which do not differ radically from the Baker values above. (In the calculations, δ^* is predicted, again, using the relation $\delta^* = (2/3\pi)\,\delta$, obtained from the laminar-flow

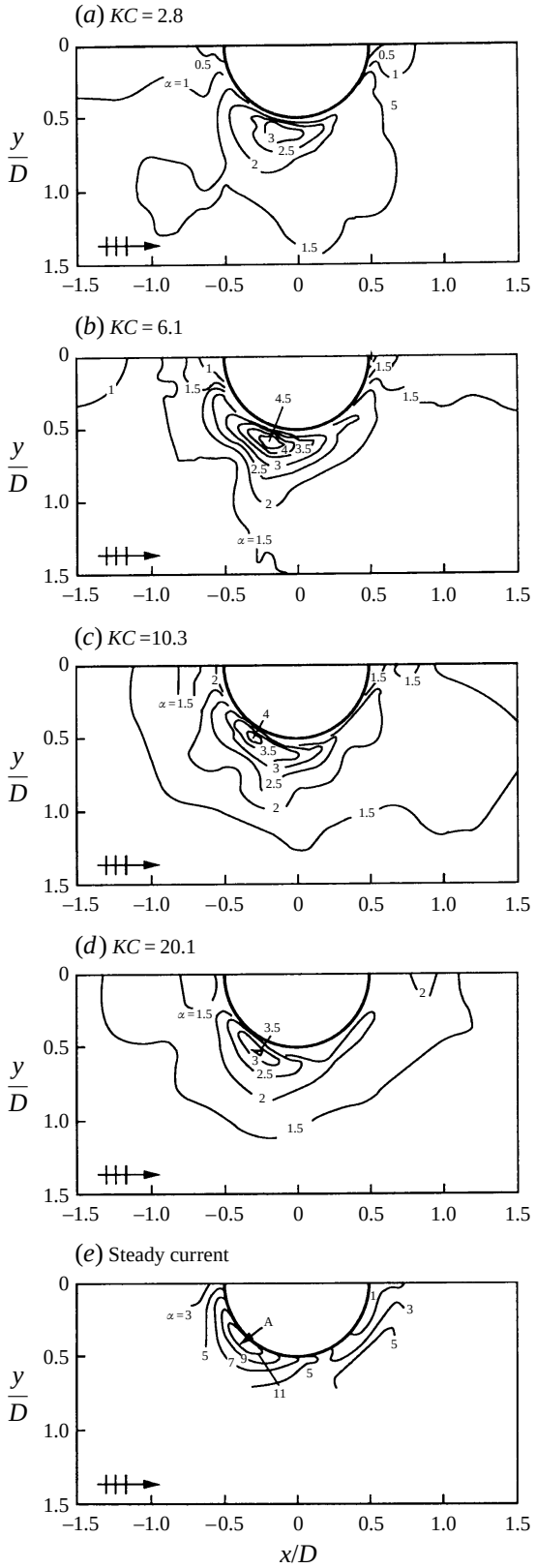
(a) KC = 2.8
(b) KC = 6.1
(c) KC = 10.3
(d) KC = 20.1
(e) Steady current
y/D
x/D
0
0.5
1.0
1.5
−1.5
−1.0
−0.5
0
0.5
1.0
1.5
α = 1
α = 1.5
α = 3
A

oscillatory boundary-layer solution (Batchelor 1967, p. 192)). However, the transition must depend not only on Re_D (or Re_{δ^*}), δ^*/D and KC, but also on the regime (laminar/turbulent) of the incoming boundary layer.

Secondly, figure 19 shows that the r.m.s. value of the fluctuations in the bed shear stress beneath the horseshoe vortex can reach values as large as the mean bed shear stress itself in the case when $KC = 20$, and it can even reach much larger values (in fact, a factor of 3–4 larger than the mean bed shear stress) in the case of a steady current. This may have significant effects on sediment transport in the process of scour around a pile placed in an erodible bed.

6. Lee-wake vortex-flow regimes

The shear layers emanating from the side edges of the pile roll up to form vortices in the lee wake of the pile (figure 1). The non-dimensional quantities describing this vortex flow depend mainly on

$$KC, \quad Re_D, \quad k_s/D, \quad \text{pile geometry}, \tag{21}$$

in which k_s is the roughness of the pile surface.

The present analysis concerns the variation with KC. The video recording of the flow around the base of the circular pile visualized by the hydrogen bubbles (figure 20) has been analysed for the crest half-period of the wave motion ($\omega t = 0°$–$180°$), to study the lee-wake flow as a function of KC. From this analysis, the following vortex-flow regimes emerged.

(*a*) $KC < 4$. Separation behind the pile occurs in the form of a pair of symmetric, attached vortices (figure 20*a*). These vortices are washed around the pile when the flow reverses.

(*b*) $4 < KC < 6$. The symmetry between the two attached vortices breaks down (figure 20*b*). (The vortices are still attached, and no shedding occurs.)

(*c*) $6 < KC < 17$. Vortex shedding first occurs when KC reaches 6. In this regime, one vortex is shed in each half-period of the waves (figure 20*c*). The attached vortices (figure 20*c*) are washed around the pile when the flow reverses. This regime corresponds to the single-pair regime of Williamson's (1985) two-dimensional sinusoidal plane oscillatory flow regimes.

(*d*) $17 < KC < 23$. In this regime, two vortices are shed in each half-period of the waves (figure 20*d*). The attached vortices are washed around the pile when the flow reverses, in the same way as in the previous regimes. This regime corresponds to the double-pair regime of Williamson's (1985) two-dimensional sinusoidal plane oscillatory flow regimes.

The present findings differ from the two-dimensional flow regimes of Williamson in only one aspect. Namely, the so-called transverse vortex street, a characteristic feature of the single-pair regime for $6 < KC < 13$ where a vortex street forms perpendicular to the direction of the motion, was not observed in the present case. This is linked to the disruption of this special vortex-flow regime in the case of real waves.

Apart from this disagreement, the present results are in accord with the results obtained for the two-dimensional free-cylinder case. This is attributed to the extremely small wave-boundary layer thickness ($\delta/D = O(0.05)$, see table 1), and therefore the

FIGURE 22. Amplification of the bed shear stress around circular pile. Steady current result is from Hjorth (1975) ($D = 7.5$ cm, $V = 30$ cm s^{-1}, h, the water depth = 20 cm).

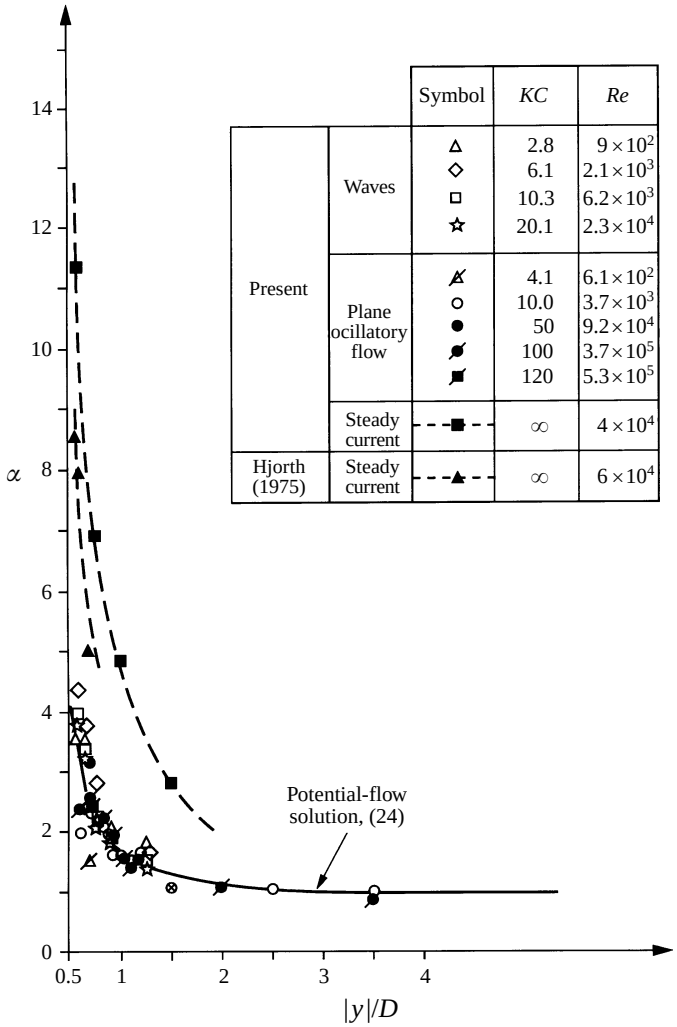

FIGURE 23. Amplification of the bed shear stress along the transverse axis. Hjorth's test conditions are as in figure 22. Open symbols, the incoming boundary layer is laminar; filled symbols, the incoming boundary layer is turbulent.

three-dimensionality of the flow is not significant as regards the development of the observed vortex-flow regimes.

Figure 21 depicts the bed shear stress distribution along the x-axis (figure 1) in the lee-wake area for various values of KC, including the steady-current case. First, the extent of the area influenced by the leewake increases with increasing KC, as expected. This agrees well with the previously described visual observations. Furthermore, it is seen that the bed shear stress in the wake increases with increasing KC. The amplification in the bed shear stress with respect to its undisturbed value can be as high as 2 for $KC = 20$ and even higher, $\mathrm{Max}\,|\bar{\tau}_0|/\tau_{0m} = O(10)$, for the case of a steady current. Finally, the bed shear stress experiences a maximum around $|x|/D \approx 1$. This is due to the contraction of the mean flow in plan view in the area between two oppositely rotating vortices emanating from the two side edges of the pile.

7. Amplification of bed shear stress

The distribution of the bed shear stress along the streamwise axis has been discussed earlier in conjunction with the horseshoe vortex (figure 17) in §5 and with the lee-wake flow (figure 21) in §6.

Figure 22 gives the full picture of the bed shear stress in the form of contour plots for various KC, including the steady-current case. The quantity α in the figure is the amplification in the bed shear stress defined by

$$\alpha = \mathrm{Max}\,|\bar{\tau}_0|/\bar{\tau}_{0m} \tag{22}$$

in the case of waves and

$$\alpha = \mathrm{Max}\,|\bar{\tau}_0|/\bar{\tau}_{0\infty} \tag{23}$$

in the case of a steady current.

First, the asymmetry observed for the wave cases (figure 22*a–d*) is due to the asymmetry between the wave crest and the wave trough.

Secondly, the figure shows that there is a concentration of bed shear stress near the side edge of the pile in the case of waves. The point where the amplification is maximum is almost at the side edge of the pile when $KC = 2.8$ while it is displaced a little upstream of the pile for other KC values. This is partly because of the wave asymmetry (figure 2) and partly because of the presence of the horseshoe vortex. In the case of a steady current, however, this point moves upstream halfway between the front and the side edges of the pile (point A in figure 22*e*). This is due to the strong presence of the horseshoe vortex in the case of a steady current.

Thirdly, while the maximum amplification of the bed shear stress is $\alpha = 3$–4 in the case of waves, it reaches values as high as 11 in the case of a steady current. In the former case, the maximum amplification in the bed shear stress is mainly due to the contraction of streamlines near the side edges of the pile. Figure 23, where α is plotted along the y-axis (figure 1) together with the potential-flow solution

$$\alpha = [1 + 0.25/(y/D)^2]^2, \tag{24}$$

supports this argument, since the wave and oscillatory-flow data agree quite well with the potential solution. On the other hand, in the steady-current case, the maximum amplification (being a factor 3 larger than the corresponding figure in waves) is due partly to the contraction of streamlines near the side edges of the pile and partly to the strong horseshoe vortex formed in front of the pile. Finally, it may be noted that the bed shear stress data presented in figure 22 may prove useful with regard to its application in the design of scour protection around piles.

8. Conclusions

(i) The horseshoe vortex formed at the bed in front of a pile exposed to waves is primarily governed by the Keulegan–Carpenter number, KC.

(ii) No horseshoe vortex exists when $KC < 6$ for a circular pile. The horseshoe vortex increases in both size and lifespan as KC is increased.

(iii) The influence of cross-sectional shape of the pile on the presence and formation of the horseshoe vortex is substantial. For a square pile with 90° orientation, the critical value of KC beyond which the horseshoe vortex comes into existence is 4, the result corresponding to the square pile with 45° orientation lies between 4 and 6.

The streamwise extent of the horseshoe vortex is largest for the square pile with 90° orientation and smallest with the square pile with 45° orientation, that corresponding to the circular pile being between the two.

Tests	T (s)	U_m (measured) (cm s^{-1})	U_{fm} (measured) (cm s^{-1})	a (cm)	$Re = \frac{aU_m}{\nu}$	δ (mm)	$KC = \frac{U_m T}{D}$	$Re_\delta = \frac{\delta U_m}{\nu}$	$Re_D = \frac{DU_m}{\nu}$
Circular pile: $D = 40$ mm									
1–16	2.2–4.4	5.1–21.5	See below	1.8–15.1	0.09–3.2×10^4	2.0–2.8	2.8–23.7	1.0–6.0×10^2	2.0–8.6×10^3
Detailed test conditions for tests where the bed shear stress is measured around the pile									
1	2.2	5.1	0.77	1.8	0.09×10^4	2.0	2.8	1.0×10^2	2.0×10^3
4	4.4	5.5	0.83	3.9	0.21×10^4	2.8	6.1	1.5×10^2	2.2×10^3
8	4.4	9.4	1.3	6.6	0.62×10^4	2.8	10.3	2.6×10^2	3.8×10^3
14	4.4	18.3	1.9	12.8	2.3×10^4	2.8	20.1	5.1×10^2	7.3×10^3
Circular pile: $D = 90$ mm									
17	1.9	31.8	2.3	9.6	3.1×10^4	1.8	6.7	5.7×10^2	2.9×10^3
Square pile (90° orientation): $D = 40$ mm									
18–32	2.2–4.4	5.1–21.5	—	1.8–15.1	0.09–3.2×10^4	2.0–2.8	2.8–23.7	1.0–6.0×10^2	2.0–8.6×10^3
Square pile (45° orientation): $D = 57$ mm									
33–47	2.2–4.4	5.1–21.1	—	1.8–15.1	0.09–3.2×10^4	2.0–2.8	2.0–16.6	1.0–6.0×10^2	2.9–12×10^3

TABLE 1. Flume experiments. Pure waves. Regime of incoming boundary layer is laminar

Tests	Pile	D (mm)	V_0 (measured) (cm s^{-1})	U_f (measured) (cm s^{-1})	δ (mm)	$Re_\delta = \frac{\delta V_0}{\nu}$	$Re_D = \frac{D V_0}{\nu}$
48	Circular	40	9.5	0.47	4.00	3.8×10^4	3.8×10^3
49	Circular	90	9.5	0.47	4.00	3.8×10^4	8.6×10^3
50, 51	Square pile with 90° orientation ($D = 40$ mm) and 45° orientation ($D = 57$ mm), respectively. Test conditions are the same as in Test 48.						

TABLE 2. Flume experiments. Steady current. Regime of incoming boundary layer is turbulent

(iv) The influence of a superimposed current on the horseshoe vortex is also significant. The effect is to increase the size and lifespan of the horseshoe vortex. This influence becomes more and more pronounced with increasing U_c/U_m, the current-to-wave-velocity ratio.

(v) The bed shear stress beneath the horseshoe vortex at the upstream edge of the pile is strongly influenced by KC. While it is of the same order of magnitude as the undisturbed-flow bed shear stress for moderate KC ($KC = O(10)$), it increases to 6–7 times the undisturbed bed shear stress as $KC \to \infty$ (i.e. in the steady-current case).

(vi) The near-bed lee-wake flow has a wide variety of vortex-flow regimes. These flow regimes, namely the symmetric vortex-pair regime ($KC < 4$), the asymmetric vortex-pair regime ($4 < KC < 6$), the single-pair regime ($6 < KC < 17$), the double-pair regime ($17 < KC < 23$), agree quite well with the corresponding two-dimensional oscillatory free-cylinder flow regimes as observed e.g. in the work of Williamson (1985). However, in the present case, no transverse vortex street was observed in the single-pair vortex regime.

(vii) Similar to the bed shear stress under the horseshoe vortex, the bed shear stress in the lee wake of the pile is also influenced by KC. While the bed shear stress in the lee-wake area is of the same order of magnitude as the undisturbed bed shear stress for $O(10) < KC < 100$, it becomes a factor 10 larger when $KC \to \infty$ (i.e. in the case of a steady current).

(viii) The amplification of the bed shear stress with respect to its undisturbed value is maximum ($O(4)$) at (or near) the side edges of the pile in the case of waves, in agreement with potential-flow theory. In the case of a steady current, however, the location of the maximum bed shear stress moves upstream along the periphery of the pile (at about 45° from the main flow direction) and the magnitude of the maximum amplification becomes $O(10)$.

This work was funded jointly by the Danish Technical Research Council (STVF) under the programme 'Marin Technique' and by the Commission of the European Communities, Directorate General for Science, Research and development, under MAST contract No. MAS2-CT92-0047, 'Monolithic (Vertical) Coastal Structures'.

Appendix

A summary of the test conditions is given in tables 1–4.

Tests	T (s)	U_m (measured) (cm s^{-1})	U_c (measured) (cm s^{-1})	$\frac{U_c}{U_m}$	a (cm)	$Re = \frac{aU_m}{\nu}$	δ (mm)	$KC = \frac{U_m T}{D}$	$Re_\delta = \frac{\delta U_m}{\nu}$ or $\frac{\delta U_c}{\nu}$	$Re_D = \frac{DU_m}{\nu}$ or $\frac{DU_c}{\nu}$
52–62	2.2–4.4	5.1–17.9	2.0–5.0	0.11–0.63	1.8–12.5	0.09–2.2 $\times 10^4$	2–2.8 (400)	2.8–20	1–5 $\times 10^4$ (0.8–2 $\times 10^4$)	2–7.2 $\times 10^3$ (0.8–2 $\times 10^3$)

TABLE 3. Flume experiments. Combined waves and current. Circular pile, $D = 40$ mm. Regime of incoming boundary layer is laminar for wave component and turbulent for current components. In the case where there are two entries, the entry in parentheses corresponds to the current component and the other to the wave component

Tests	U_m (measured) (cm s^{-1})	U_{fm} (measured) (cm s^{-1})	a (cm)	$Re = \frac{aU_m}{\nu}$	δ (mm)	$KC = \frac{U_m T}{D}$	$Re_\delta = \frac{\delta U_m}{\nu}$	$Re_D = \frac{DU_m}{\nu}$	Regime of incoming boundary layer flow
63	1.9	—	3.2	6.1×10^2	4.3	4.1	0.8×10^2	9.5×10^2	Laminar
64	4.6	0.61	8.0	3.7×10^3	4.4	10	2.0×10^2	2.3×10^3	Laminar
65	23.1	—	39.8	9.2×10^4	4.4	50	1.0×10^3	1.2×10^4	Laminar
66	46.3	2.5	79.6	3.7×10^5	11.4	100	5.3×10^3	2.3×10^4	Transitional
67	55.6	—	95.5	5.3×10^5	15.0	120	8.3×10^3	2.8×10^4	Transitional

TABLE 4. Water-tunnel experiments. Pure oscillatory flow. Circular pile, $D = 50$ mm. Flow period $T = 10.8$ s

REFERENCES

BAKER, C. J. 1979 The laminar horseshoe vortex. *J. Fluid Mech.* **95**, 347–367.

BAKER, C. J. 1985 The position of points of maximum and minimum shear stress upstream of cylinders mounted normal to flat plates. *J. Wind Engng Indust. Aerodyn.* **18**, 263–274.

BAKER, C. J. 1991 The oscillation of horseshoe vortex systems. *Trans. ASME I: J. Fluids Engng* **113**, 489–495.

BATCHELOR, G. K. 1967 *An Introduction to Fluid Dynamics*. Cambridge University Press.

BEARMAN, P. W., GRAHAM, J. M. R., NAYLOR, P. & OBASAJU, E. D. 1981 The role of vortices in oscillatory flow about bluff cylinders. In *Proc. Intl Symp. on Hydrodyn. in Ocean Engng, Trondheim, Norway* (ed. K. M. Gisvold *et al.*). Norwegian Hydrodynamic Laboratories, Norwegian Institute of Technology

BELIK, L. 1973 The secondary flow about circular cylinders mounted normal to a flat plate. *Aero. Q.* February, 47–54.

BRILEY, W. R. & MCDONALD, H. 1981 Computation of three dimensional horseshoe vortex flow using the Navier-Stokes equations. *Proc. 7th ICNMFD, Stanford, CA* (ed. W. C. Reynolds & R. W. MacCormack). Lecture Notes in Physics, vol. 141 Springer.

DARGAHI, B. 1989 The turbulent flow field around a circular cylinder. *Exps. Fluids* **8**, 1–12.

DENG, G. B. & PIQUET, J. 1992 Navier-Stokes computations of horseshoe vortex flows. *Intl J. Numer. Meth. Fluids* **15**, 99–124.

DRIEST, E. R. VAN 1956 On turbulent flow near a wall. *J. Aero. Sci.* **23**, 1007–1011.

HJORTH, P. 1975 Studies on the nature of local scour. *Dept. of Water Resources Engng, Lund Inst. of Technology, Univ. of Lund, Sweden, Bull Series* A 46.

JENSEN, B. L., SUMER, B. M. & FREDSØE, J. 1989 Turbulent oscillatory boundary layers at high Reynolds numbers. *J. Fluid Mech.* **206**, 265–297.

KOBAYASHI, T. 1992 Three-dimensional analysis of the flow around a vertical cylinder on a scoured seabed. *Intl Conf. on Coastal Engineering, 4–9 October 1992, Venice, Italy* (ed. B. L. Edge). ASCE.

KWAK, D., ROGERS, S. E., KAUL, U. K. & CHANG, J. L. C. 1986 A numerical study of incompressible juncture flows. *NASA Tech. Mem.* 88319. Ames Research Center, Moffet Field, CA 94035.

LONGUET-HIGGINS, M. S. 1957 The mechanics of the boundary-layer near the bottom in a progressive wave. Appendix to 'An experimental investigation of drift profiles in a closed channel' by R. C. H. Russell & J. D. C. Osorio. *Proc. 6th Intl Conf. Coast. Eng., Miami, FL.*, pp. 184–193.

NIEDORODA, A. W. & DALTON, C. 1982 A review of the fluid mechanics of ocean scour. *Ocean Engng* **9**, 159–170.

SARPKAYA, T. 1986 Force on a circular cylinder in viscous oscillatory flow at low Keulegen–Carpenter numbers. *J. Fluid Mech.* **165**, 61–71.

SARPKAYA, T. & ISAACSON, M. 1981 *Mechanics of Wave Forces on Offshore Structures*. Van Nostrand Reinhold.

SCHWIND, R. 1962 The Three-dimensional boundary layer near a strut. *Gas turbine Lab., Rep.* 67. MIT.

SLEATH, J. F. A. 1984 *Sea Bed Mechanics*. John Wiley and Sons.

SUMER, B. M., ARNSKOV, M. M., CHRISTIANSEN, N. & JØRGENSEN, F. E. 1993 Two-Component hot-film probe for measurements of wall shear stress. *Exps. Fluids* **15**, 380–384.

WILLIAMSON, C. H. K. 1985 Sinusoidal flow relative to circular cylinders. *J. Fluid Mech.* **155**, 141–174.